ACS APPLIED MATERIALS & INTERFACES

www.acsami.org Research Article

Spongy Ag Foam for Soft and Stretchable Strain Gauges

Seokkyoon Hong,[▽] Haozhe Zhang,[▽] Junsang Lee,[▽] Tianhao Yu, Seungse Cho, Taewoong Park, Julia Walsh, Yuhyun Ji, Joshua Jeremiah Kim, Hyowon Lee, Dong Rip Kim,* Baoxing Xu,* and Chi Hwan Lee*

Cite This: https://doi.org/10.1021/acsami.4c04719 Read Online

ACCESS | Metrics & More | Article Recommendations | Supporting Information

ABSTRACT: Strain gauges, particularly for wearable sensing applications, require a high degree of stretchability, softness, sensitivity, selectivity, and linearity. They must also steer clear of challenges such as mechanical and electrical hysteresis, overshoot behavior, and slow response/recovery times. However, current strain gauges face challenges in satisfying all of these requirements at once due to the inevitable trade-offs between these properties. Here, we present an innovative method for creating strain gauges from spongy Ag foam through a steam-etching process. This method simplifies the traditional, more complex, and costly manufacturing techniques, presenting an eco-friendly alternative. Uniquely, the strain gauges crafted from this method achieve an unparalleled gauge factor greater than 8×10^3 at strains exceeding 100%, successfully meeting all required attributes without notable trade-offs. Our work includes systematic investigations that reveal the intricate structure−property−performance relationship of the spongy Ag foam with practical demonstrations in areas such as human motion monitoring and human−robot interaction. These breakthroughs pave the way for highly sensitive and selective strain gauges, showing immediate applicability across a wide range of wearable sensing applications.

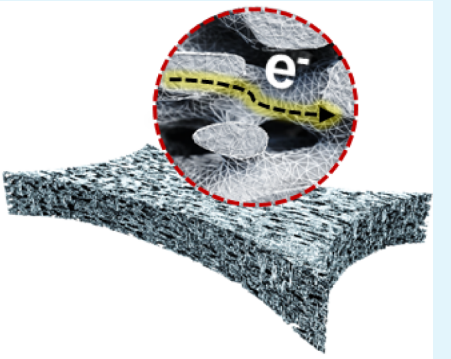

KEYWORDS: *spongy foam, strain gauge, steam etching, nanowires, wearable sensors*

INTRODUCTION

Strain gauges that are soft and stretchable are of particular interest in wearable sensing applications, such as human motion monitoring and human−robot interaction, owing to their ability to effectively accommodate external strains of up to 50% or more on the skin.[1−5] Most of these strain gauges are usually constructed using elastomers that contain various forms of conductive nanomaterials, such as particles,[6−8] tubes,[9−11] wires,[12−14] films,[15−17] flakes,[18,19] and shells,[20,21] which cause a shift in resistance when stretched. The shift is originated from the disconnection and reconstruction of electrical network formed by the conductive materials,[22] and the modification of types, size, and concentration of the conductive materials facilitates the fine-tuning of performance in stretchable devices.[22−24] For reliable sensing, these strain gauges require a high degree of stretchability, softness, sensitivity, selectivity, and linearity, while avoiding mechanical and electrical hysteresis, overshoot behavior, and slow response/recovery time.[25,26] Efforts to enhance sensor performance have been pursued through considerations of various aspects, including the combination of materials, microstructural modifications, and interfacial stability between elastomers and conductive materials.[24−28] Despite significant advances, satisfying all of these essential features without any trade-offs continues to be a challenge.

Here, we introduce strain gauges made of a spongy Ag foam that provides an unparalleled gauge factor of $>8 \times 10^3$ at a large strain of >100%, while retaining all of the requirements without notable trade-offs. The spongy Ag foam is highly porous at the microscale and contains percolation networks of Ag nanowires (NWs) as internal conducting passages, providing the following features at the same time: (1) stretchability over 100% without mechanical failures; (2) softness with an elastic modulus (E) of ∼0.9 MPa; (3) selectivity to stretching that is decoupled from other deformation modes such as compression and bending; (4) linearity versus tensile strains (R^2 = 0.997); (5) suppressed mechanical and electrical hysteresis (14% and 11%) under >1,000 cycles of loading/unloading; (6) negligible overshoot behavior; and (7) fast response and recovery time (266 and 292 ms). These qualities are crucial for advancing wearable sensing technologies that require strain gauges with such comprehensive performance capabilities. This work involves systematic investigations to explore the structure−property−

Received: March 21, 2024
Revised: May 5, 2024
Accepted: May 6, 2024

performance relationship of the spongy Ag foam compared to other stretchable strain gauges, as summarized in Table S1. Proof-of-concept demonstrations include the use of the spongy Ag foam for human motion monitoring, such as detecting facial expressions, speaking, coughing, drinking, joint bending, muscle contraction, respiration rate, and blinking from the skin of various body parts. Additionally, the sensing data can be utilized for human−robot interactions to coordinate robot fingers and express sign languages. These collective results highlight the broad spectrum of utilizing spongy Ag foam in wearable sensing applications.

RESULTS AND DISCUSSION

Design Configuration and Fabrication Method. Figure 1a schematically illustrates the spongy Ag foam, which is highly

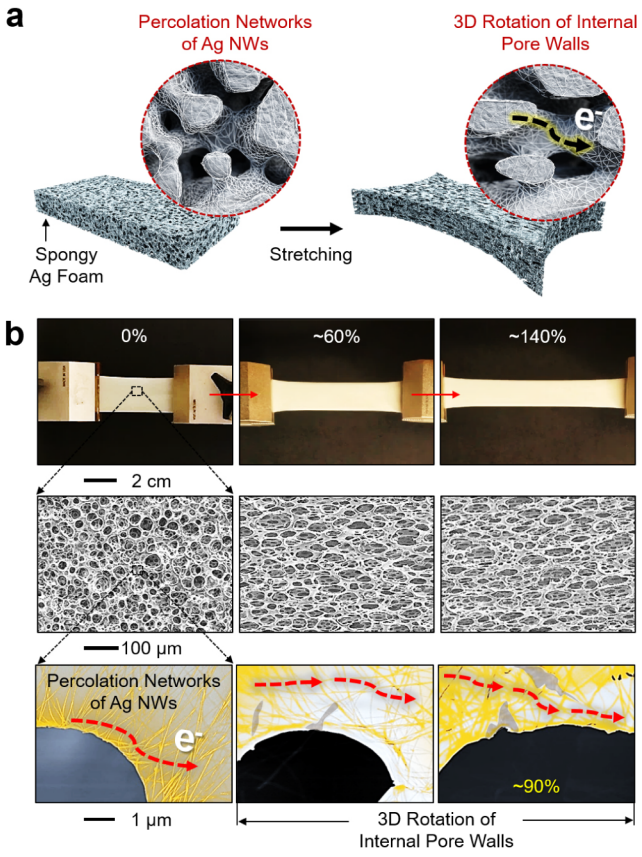

Figure 1. Design configuration of the spongy Ag foam under stretching. (a) Schematic illustration of the spongy Ag foam, with enlarged insets highlighting the percolation networks of Ag NWs as internal conducting passages. (b) Photographs and SEM images of the spongy Ag foam under stretching, with colored images highlighting the percolation networks of Ag NWs.

porous and contains percolation networks of Ag NWs as internal conducting passages. The corresponding photographs and scanning electron microscopy (SEM) images of the spongy Ag foam under stretching are shown in Figure 1b. The spongy Ag foam exhibited elasticity of over 100%, without causing notable damage, due to the three-dimensional (3D) rotation of its internal pore walls to accommodate deformations.[29−31] The spongy Ag foam was also bendable, compressible, and able to withstand torsion without compromising its material properties (Movie S1).

The spongy Ag foam was produced through a unique steam-etching process using a universal pressure rice cooker that can generate a large number of highly perforated and randomly distributed micropores, with diameters ranging from 5 to 50 μm (Figure S1). The porosity of the spongy Ag foam exceeded 80%, surpassing the typical porosity of less than 60% found in other ordered porous structures defined by lithography.[32] The higher porosity of the spongy Ag foam leads to a substantially increased internal surface area. This, in turn, enhances deformability, sensitivity, breathability, and stability, which makes the spongy Ag foam suitable for strain sensing applications.[33,34] The steam-etching process is rapid and can complete a batch of size 4 × 3 in^2 within 30 min. Moreover, the steam-etching process is an ecofriendly fabrication that uses pressurized water molecules to induce the formation of highly interconnected inner pores in elastomers. While there exist other conventional fabrication methods to create porous elastomers, such as lithography, templating, and 3D printing, each comes with its own set of drawbacks. While lithography and templating involve challenging template removal processes, high costs, and the use of hazardous solvents, 3D printing can be expensive and time-consuming, thus compromising fabrication efficiency (Table S2).[35−39] Furthermore, although there has been research exploring the infiltration of CNTs into porous elastomers fabricated by conventional methods, to our knowledge, no studies have yet investigated strain sensors utilizing percolated networks of Ag NWs within such elastomers.[30] The steam-etching process began by spin-casting an uncured elastomer, such as poly(dimethylsiloxane) (PDMS), on a glass slide with a base to cross-linker ratio of 10:1 v/v and a target thickness in the range of 100−200 μm. The elastomer was then cured in a pressure rice cooker (Instant Pot Duo; Instant Brands, Inc.) with pressurized hot steam at 120 °C and 15 psi, resulting in the formation of highly perforated and randomly distributed micropores. These micropores were mainly formed due to the pressurized water molecules penetrating and evaporating from the uncured elastomer.[40] Pressure rice cooker was used to control the steam-etching conditions, with a temperature range of 110−120 °C and a pressure range of 5.8−15 psi. No notable variations in the overall porosity of the spongy Ag foam were detected within these ranges in the entire region, as shown in Figure S2 and summarized in Table S3. The cured elastomer was then immersed in a 1 mg mL^{-1} solution of Ag NWs, leading to infiltration of the Ag NWs into the perforated micropores (Figure S1). The spongy Ag foam could be patterned into the desired shape using a shadow mask during the step of forming the micropores (Figure S3).

Multidimensional Mechanics. The spongy Ag foam, owing to the 3D rotation of its internal pore walls, remains effectively responsive to stretching without being affected by other deformation modes, such as compression and bending. Figure 2 presents the representative results of a 3D finite element analysis (FEA) displaying the distribution of strains in the spongy Ag foam under stretching, compression, and bending. The spongy Ag foam was modeled with a porosity of 25%, 50%, and 75%, consisting of interconnected pores in the form of randomly positioned spherical shapes. The accompanying visual representations of the spongy Ag foam under these deformations are shown in Movie S2. The internal pore walls experienced the largest strains, which can be attributed to stress concentration during stretching as compared to compression and bending. Upon stretching, the internal pore

https://doi.org/10.1021/acsami.4c04719
ACS Appl. Mater. Interfaces XXXX, XXX, XXX−XXX

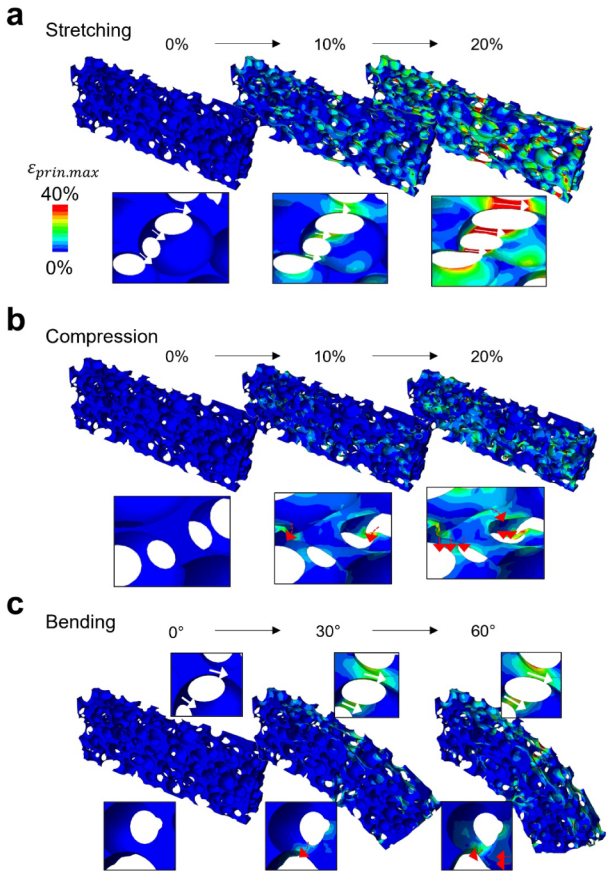

Figure 2. 3D FEA results depicting the mechanical behavior of the spongy Ag foam under various loading conditions. (a) stretching up to 20%, (b) compressing up to 20%, and (c) bending up to 60°. The insets show the local stress concentration and deformation behavior of the spongy Ag foam under each load condition.

walls rotated and aligned themselves in the direction of the stretch (Figure 2a, inset). Subsequent stretching caused localized tensile strains on the walls, leading to a noticeable rise in the resistance. Upon compression, the internal pore walls were crushed, leading to a reduction in pore size and a relatively low concentration of strains, with the exception of areas where the walls were bent (Figure 2b, inset). Upon bending, the spongy Ag foam exhibited deformation behaviors similar to stretching and compression above and below the neutral plane, respectively (Figure 2c, inset).

The corresponding results of the spongy Ag foam with different porosities are shown in Figure S4. Upon stretching, the increased porosity resulted in a larger area experiencing minimal strain due to the concentration of strain in small regions where the pore walls were parallel to the loading axis. As porosity increases, the region experiencing negligible strain levels expands, resulting in an increased mechanical compliance. Additionally, it is anticipated that the rate of variation in electrical resistance with strain will decrease in accordance with the increase in porosity, aligning with the observed mechanical characteristics. Thus, higher porosity leads to enhanced softness, deformability, and selectivity, making highly porous characteristics of spongy Ag foams ideal for achieving optimal strain sensing performance. Upon compression and bending, the increased porosity allowed materials to move into the empty spaces, resulting in minimal strain and reduced lateral deformation, ultimately leading to a negligible Poisson effect. These findings are consistent with the results obtained from 2D FEA, demonstrating that the internal pore walls have increased rotational and bending capabilities (Figure S5). Upon stretching, the maximum principal strain (ε_{max}) remained below 40%, while it was less than 10% and 5% upon compression and bending, respectively. The presence of high porosity (>75%) in the spongy Ag foam substantially reduced the concentration of local stress and deformation upon bending and compression, leading to an insensitivity to these loadings.

Softness, Stretchability, Sensitivity, and Linear Responsivity. Figure 3a presents the stress−strain curve of

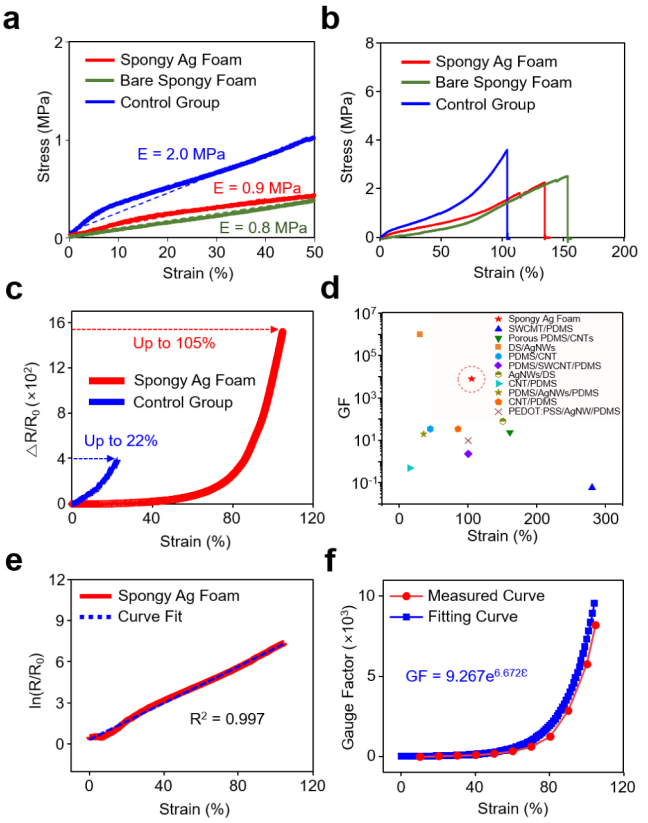

Figure 3. Softness, stretchability, sensitivity, and linear responsivity. (a) Stress−strain curves of the spongy Ag foam (red line), bare spongy foam without Ag NWs (green line), and control group (blue line), indicating the mechanical moduli. (b) Stress−strain curves of the spongy Ag foam, bare spongy Ag foam, and control group, indicating the fracture strain. (c) $\Delta R/R_0$ of the spongy Ag foam and control group with strain. (d) Comparison of GF and maximum working strain range among various stretchable strain gauges. (e) Linear relationship of the spongy Ag foam with strain. (f) Comparison of fitting and measured GF with strain for the spongy Ag foam.

the spongy Ag foam (in red) compared to the bare spongy foam without Ag NWs (in green) and a control group that features a network of Ag NWs atop a nonporous PDMS substrate (in blue). Schematic illustrations of the control group are shown in Figure S6. Both the spongy foam with and without Ag NWs exhibited a nearly 2-fold decrease in stiffness compared to the control group, with corresponding mechanical moduli of 0.9 and 2.0 MPa, respectively. Additionally, the spongy foam with and without Ag NWs displayed a superior tensile breaking strain of >140% and >150%, respectively, compared to that (>100%) of the control group (Figure 3b).

https://doi.org/10.1021/acsami.4c04719
ACS Appl. Mater. Interfaces XXXX, XXX, XXX−XXX

These are primarily due to the 3D rotation of the internal pore walls relative to the stretching direction, resulting in lower local strains acting on the Ag NWs.[29−31] The relative resistance change ($\Delta R/R_0$) of the spongy Ag foam increased exponentially at the applied strain of >100%, where the corresponding sensing range remained higher, by >4-fold, than that (up to 22%) of the control group (Figure 3c). The microporous structure of the spongy Ag foam had a larger portion of its volume exposed to lower levels of strains compared to the nonporous structure, resulting in a slower increase in resistance and a drastically increased strain-sensing range (Figure S7). Notably, the R and $\Delta R/R_0$ of the spongy Ag foam were substantially lower and higher, by >11,000-fold and >140-fold, relative to those of a similar spongy foam containing multiwalled carbon nanotubes (MWCNTs), respectively (Figure S8). Moreover, the strain-sensing range and $\Delta R/R_0$ of the spongy Ag foam remained consistent regardless of the size of the sensor (Figure S9). Furthermore, the electrical characteristics of the spongy Ag foam can be controlled by adjusting the concentration of Ag NWs. For instance, a higher concentration of Ag NWs results in a lower initial resistance of up to 33 Ω and a larger strain-sensing range of over 100% in the spongy Ag foam. (Figure S10). Accordingly, we selected the Ag NW concentration of 0.5 wt % as the optimal concentration.

The superior sensitivity of the spongy Ag foam compared to the MWCNTs foam can be attributed to the relatively low fracture toughness of Ag NWs.[41] This property leads to a substantial increase in resistance as the highly percolated Ag NWs undergo strain. For comparison, Figure S11 shows representative images of cracks and delamination that occurred in the control group when it was stretched to >5% and >22%, respectively. On the contrary, the spongy Ag foam exhibits the formation of microcracks in Ag NWs with no signs of delamination between the Ag NWs and the spongy foam (Figure 1b). This is largely due to stress dissipation across the spongy Ag foam, facilitated by the three-dimensional rotation of its internal pore walls. Such mechanics allow the spongy Ag foam to undergo deformations with a reduced effective strain on the interconnected pore walls, thereby enabling the percolation network of Ag NWs to adjust flexibly along the surface without delamination during mechanical deformation. As a result, the spongy Ag foam exhibited an unprecedentedly high gauge factor (GF > 8×10^3) at a large strain of >100% compared to other stretchable strain gauges (Figure 3d).[9,30,41−49] Besides, the spongy Ag foam maintained a high linearity ($R^2 = 0.997$) in response to strains of >100% (Figure 3e). The fitting and measured curves of GF matched well each other for precision calibration (Figure 3f).[50]

Suppressed Hysteresis, Negligible Overshoot Behavior, and Rapid Response/Recovery Time. For wearable sensing applications, the spongy Ag foam must operate stably under cyclic loads without causing any damage or deterioration. Figure 4a shows the spongy Ag foam showed no notable alteration in $\Delta R/R_0$ against >1,000 cycles of stretching at an applied strain of up to 5%, in contrast to the control group, which experienced a more than 4-fold increase in $\Delta R/R_0$. The findings remained consistent for strains up to 50% over 2,000 cycles (Figure S12). In contrast, the control group could not be assessed at these strain levels as the perforated networks of Ag NWs exhibited cracks and buckling (Figure S13). Figure 4b presents that the mechanical hysteresis (H_M) of the spongy Ag foam remained lower than that of the control group when

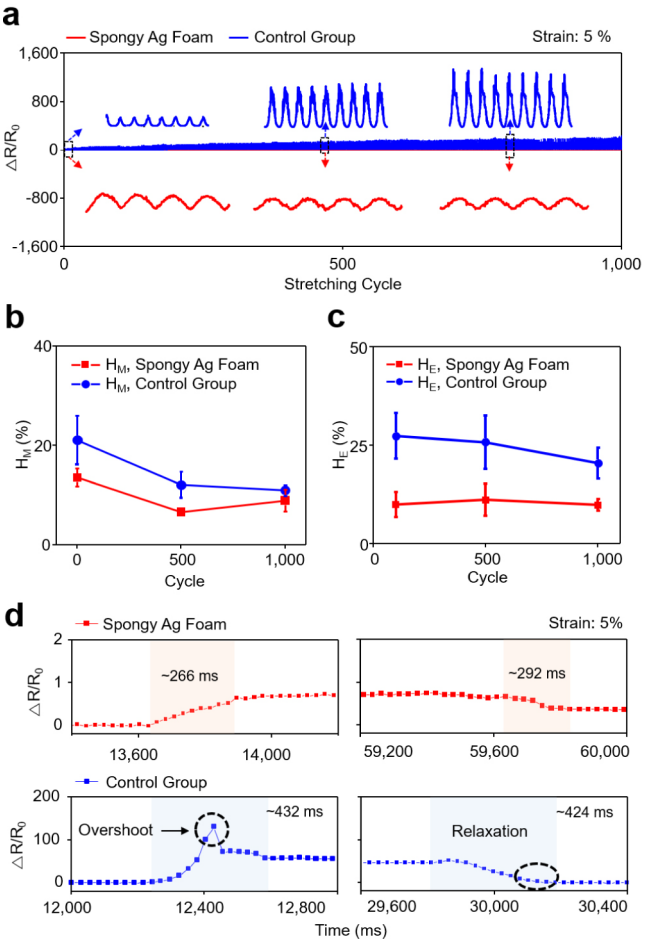

Figure 4. Suppressed hysteresis, negligible overshoot behavior, and rapid response/recovery time. (a) $\Delta R/R_0$ of the spongy Ag foam (red line) and control group (blue line) throughout 1,000 stretching−releasing cycles with a strain of 5%. (b) H_M of the spongy Ag foam and control group. (c) H_E of the spongy Ag foam and control group. (d) Response/recovery time of the spongy Ag foam and control group.

stretched more than 1,000 cycles due to the reduced viscoelasticity of the elastomer (i.e., PDMS) caused by the presence of the highly perforated micropores. The H_M decreased in the first cycle due to an initial hysteresis effect (i.e., irreversible plastic deformation) and then remained stable during subsequent cycles (i.e., reversible elastic deformation).[51] Similarly, the electrical hysteresis (H_E) of the spongy Ag foam remained lower than that of the control group in response to the stretching cycles due to the reversible elastic deformation of the micropores (Figure 4c).[52] The results maintained consistency for strains of up to 50% (Figure S14). Further measurement data for H_M and H_E are depicted in Figure S15.

Figure 4d presents the response (left column) and recovery (right column) times of the spongy Ag foam (top row) compared to the control group (bottom row) at a strain of 5%, with a loading and unloading rate of 500 mm min^{-1}. The response and recovery time of the spongy Ag foam were measured as ∼266 ms and ∼292 ms with the corresponding latency of 26 and 52 ms, respectively. These response and recovery time were at least 1.6-fold and 1.5-fold faster than those observed in the control group and prior studies,

https://doi.org/10.1021/acsami.4c04719
ACS Appl. Mater. Interfaces XXXX, XXX, XXX−XXX

respectively.[41−43] As the strain increased to 10%, 30%, and 50%, the response/recovery times also increased to approximately 317/340, 793/672, and 1.084/0.879 s, respectively (Figure S16). In addition, no notable overshoot or relaxation behavior was observed for the spongy Ag foam up to a strain of 50%, in contrast to the control group at a strain of 5%, which was typically reported in prior studies due to the viscoelastic nature of elastomers.[53−55]

Selective Responsivity to Stretching. The spongy Ag foam is selectively responsible for stretching that is decoupled from other deformations, such as compression and bending, due to its highly porous structure and percolated network of the Ag NWs. For example, the micropores of the spongy Ag foam can be closed when compressed or bent without substantially altering the percolation pathways of the Ag NWs, resulting in minimal resistance changes. Figure 5a presents that the $\Delta R/R_0$ of the spongy Ag foam remained barely changed under the pressure and after undergoing more than 1,000 cycles of bending at 90°. Moreover, the $\Delta R/R_0$ of the spongy Ag foam remained almost unchanged when compressed with a weight of 1 kg over several hours and at various bending radius (Figure S17). Figure 5b demonstrates consistent results, even under harsh hammering and folding, as illustrated in Movie S3. As another demonstration, a "P"-shape-patterned spongy Ag foam was used as a power connector to a light-emitting diode (LED) when subjected to compression up to 10 kPa, bending up to 90°, and stretching up to 60% (Figure S18a). The light intensity of the LED barely changed upon compression and bending but experienced an abrupt decrease upon stretching (Figure S18b). Real-time demonstrations of these cases are shown in Movie S4. Collectively, these findings indicate the remarkable ability of the spongy Ag foam to effectively isolate stretching from compression and bending.

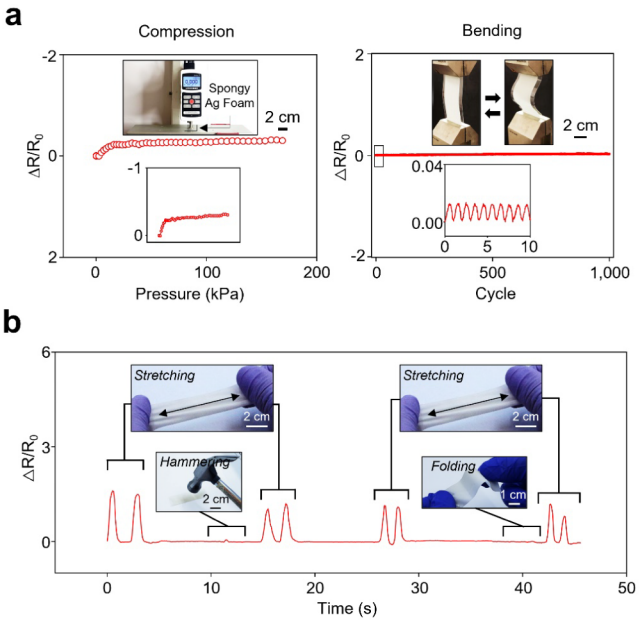

Figure 5. Selective responsivity to stretching. (a) $\Delta R/R_0$ observed in the spongy Ag foam during compression and bending. (b) Selective response of the spongy Ag foam to stretching compared to other deformation modes, with insets showcasing its behavior under stretching, hammering, and bending.

Proof-Of-Concept Demonstrations in Wearable Sensing Applications. Strain gauges that can be flexibly adhered on the skin have been utilized to track human motion and human−robot interaction in real time, providing valuable information on the magnitude, intensity, and consistency of the strains imposed on muscles or joints.[56] This information can have a significant impact on various aspects of healthcare and human performance. Some of the examples include (1) injury prevention through real-time alerts on potentially harmful movements or excessive strain,[57] (2) personalized rehabilitation, allowing medical professionals to monitor progress and adjust treatment plans based on the specific needs of each patient,[58] (3) improved pain management by gaining insights into the root causes of chronic pain through ongoing monitoring of joint and muscle forces,[59] and (4) accurate gait analysis, which is crucial in the diagnosis and treatment of conditions such as cerebral palsy, multiple sclerosis, and Parkinson's disease.[60] To showcase examples of the spongy Ag foam for motion tracking, multiple prototypes were designed to measure strain changes ranging from minor (0−5%) to substantial (5−50%) in various body parts, including the facial muscles, neck during speaking, coughing, and drinking, joints during bending, upper arms during muscle contractions, abdomen for measuring respiration rate, and eyelids during blinking, from a participant (Figure 6a). The spongy Ag foam showed a detectable change in resistance when responding to skin deformations or vibrations caused by various body motions (Figure 6b). Real-time demonstrations of these cases are shown in Movie S5. For a further demonstration of human−robot interaction, the bending of finger joints was tracked and processed using a single-board microcontroller to coordinate robot fingers in expressing sign language words, such as "peace," "love," and "rock" (Figure 6c). Real-time demonstrations of these cases are shown in Movie S6. Importantly, no signs of skin irritation were observed during these demonstrations (Figure S19). Details of skin irritation testing can be found in the Experimental Section. Furthermore, the time-dependent cell viability of the spongy Ag foam to human pulmonary arterial endothelial cells (HPAEC) was assessed to identify any adverse response at the cellular level (Figure S20). Specifically, HPAEC were cultured in vascular cell basal medium with a VEGF growth supplement (ATCC, PCS-100−041) at 37.5 °C for 24 to 48 h. The cells were seeded on the surface of the spongy Ag foam and measured using MTT (3-(4,5-dimethylthiazol-2-yl)−2,5-diphenyltetrazolium bromide) and Neutral Red (NR) assay kits (Abcam, ab211091 and ab234039 respectively). Details of the cell viability are described in the Experimental Section. Figure S20a shows the experimental results obtained from the spongy Ag foam (red bars) as compared to those of its bare cells (blue bars). The cell viability of the spongy Ag foam remained above 95% throughout the assay period without notable differences among the groups using an MTT assay (n = 9 for each group). The results closely resemble those obtained from an NR assay (Figure S20b).

CONCLUSION

This study proposes an innovative method for producing a spongy Ag foam through a rapid and straightforward steam-etching process using a universal pressure rice cooker. The spongy Ag foam offers a remarkable balance between stretchability, softness, sensitivity, selectivity, linearity, mechanical/electrical hysteresis, overshoot behavior, and response/

https://doi.org/10.1021/acsami.4c04719
ACS Appl. Mater. Interfaces XXXX, XXX, XXX−XXX

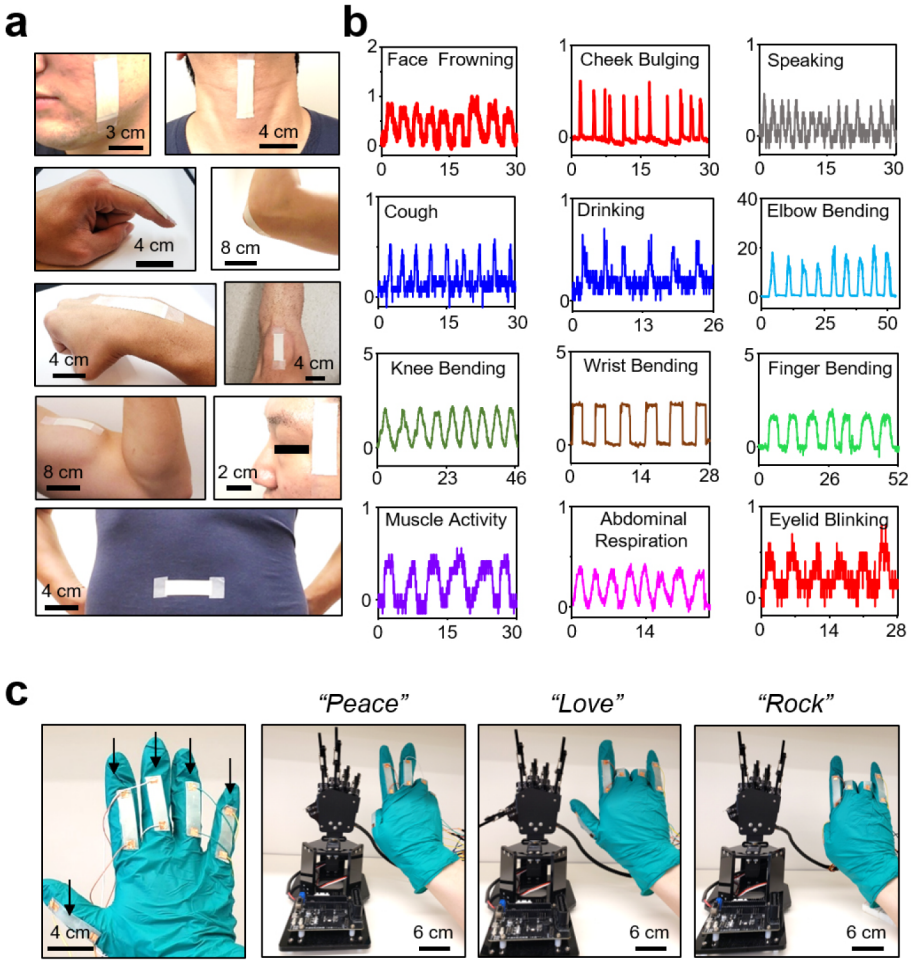

Figure 6. Proof-of-concept demonstrations in wearable sensing applications. (a) Photographs of the spongy Ag foam attached to different body parts. (b) Detection of skin deformations or vibrations from the attached body parts. (c) Demonstration of human−robot interaction using a glove with the spongy Ag foam attached to a human hand.

recovery time, making it suitable for wearable strain gauges. With its distinctive microporous structure, the spongy Ag foam achieves a record-breaking GF of >8 × 10^3 at a large strain of >100%, surpassing the performance of other stretchable strain gauges. The remarkable characteristics of the spongy Ag foam allow for accurate detection of strain levels across a wide range, from subtle to significant, for a range of wearable sensing applications, including human motion monitoring and human−robot interactions. Modifying the control system of the robotic arm for more gradual movements to mirror the linearity of the sensor offers a promising pathway for improving robotic systems, a direction intended for investigation in upcoming research endeavors. Establishing solid interface between conductive materials and elastomers could further advance the development of a robust conductive network, thus enabling expanded applications and enhanced performance in wearable sensing technologies.

EXPERIMENTAL SECTION

Materials. The average diameter and length of the Ag NWs (Flexioink; SG Flexio, Inc.) were measured as 20−25 nm and 20−25 μm, respectively. The average diameter and length of the MWCNTs (Cheaptubes. Inc.: purity >95 wt %) were measured as 10−20 nm and 10−30 μm, respectively. The MWCNTs were blended with isopropanol at a weight ratio of 0.5 wt % and sonicated for an hour to produce a uniform suspension through untangling.

Fabrication Setup for Steam Etching. A setup for a pressure rice cooker (Instant Pot Duo; Instant Brands, Inc.) is composed of a steam-etching chamber containing boiling water of 500g or more and a platform that supports the PDMS substrate above the water level (Figure S21a). The PDMS substrate was positioned in the center of the steam-etching chamber on the top of the supporting platform so that the elastomer is exposed to the steam within the interior of the steam-etching chamber. The steam-etching chamber is brought to a temperature of 120 °C that exceeds the boiling point of water such that the interior of the steam-etching chamber is filled with steam. The air within the steam-etching chamber is brought to an internal pressure of 15 psi that exceeds atmospheric pressure, provided that the temperature of the steam-etching chamber still exceeds the boiling point of water. Such a steam-etching step is carried out at a temperature of 120 °C with a pressure of 15 psi for 15−30 min, for a batch size of approximately 4 × 3 inches. A shadow mask defining a cutout pattern is disposed on top of the layer of elastomer, such that only the portions of the elastomer that are within the cutout pattern are exposed to steam. This mask layer is shown in Figure S21b, which shows a shadow mask defining a cutout design that resembles a letter "P" and that exposes only the portions of the elastomer layer to form porous structures that are within that design.

Fabrication of the Spongy Ag Foam. An uncured PDMS precursor in a mixture of 10:1 weight ratio of base and curing agents was spin-cast onto a glass substrate. The PDMS was cured in a pressure rice cooker (Instant Pot Duo; Instant Brands, Inc.) with a steam temperature of 120 °C and pressure of 15 psi to create perforated micropores with diameters ranging from 5 to 50 μm.

https://doi.org/10.1021/acsami.4c04719
ACS Appl. Mater. Interfaces XXXX, XXX, XXX−XXX

During this step, a shadow mask with the desired design was placed on top of the PDMS surface for patterning. It was then subjected to oxygen plasma for 10 min to create a hydrophilic surface. Then, oxygen plasma-treated PDMS was then immersed in a 1 mg mL^{-1} solution of Ag NWs in a vacuum chamber over 8 h to facilitate the infiltration of the Ag NWs into the perforated micropores. This facilitated the absorption and deposition of the Ag NWs throughout the perforated micropores. The PDMS was spin-cast to eliminate any residual Ag NWs on its surface and then dried in ambient conditions. The resulting spongy Ag foam was cut to the desired size for use.

Finite Element Analysis (FEA). A commercially available standard software, the ABAQUS package, was used for FEA. The spongy Ag foam was modeled with different porosities of 25%, 50%, and 75% and randomly located with spherical shapes interconnected with other pores. The spongy Ag foam, made of PDMS, was modeled with a Neo-Hookean hyperelastic model using uniaxial tension test results and a Poisson's ratio (ν) of 0.45. Strain values exceeding the maximum strain contours of 40% and 20% were colored red to aid in visual analysis.

Mechanical and Electrical Characterizations. The spongy Ag foam was cut to a size of 2 × 7.5 cm for mechanical testing using a mechanical testing system (Mark-10) to obtain its stress−strain curve. The resistance of the spongy Ag foam was measured by using a source meter (Keithley 2400; Tektronix, Inc.) in a two-wire configuration for electrical testing. The resistance of the spongy Ag foam was evaluated after 10 days when the oxidation effect of Ag NWs was negligible (Figure S22). The spongy Ag foam exhibited increased resistance change at high humidity condition (95%) and high temperature (80 °C) for 10 days due to its oxidation (Figure S23). The structural details of the spongy Ag foam were analyzed using high-resolution SEM (S-4800; Hitachi, Inc.).

Gauge Factor (GF). Gauge factor is defined by the following eq 1:

$$GF = \left(\frac{\Delta R}{R_0}\right)\Big/\varepsilon \tag{1}$$

where R_0, ΔR, and ε are the initial resistance before stretching, difference of resistance under stretching, and applied strain, respectively. The GF of the spongy Ag foam was obtained from a linear fitting ($GF = 9.267 \bullet e^{6.672\varepsilon}$) divided by each strain of 10% and compared with that of the control group. The relative resistance change ($\Delta R/R_0$) with respect to the applied strain can be calculated with the following eq 2:

$$\frac{\Delta R}{R_0} = Ae^{B\varepsilon} \tag{2}$$

In eq 2, $\ln(\Delta R/R_0) = 6.672 \bullet \varepsilon + 0.3286$ was obtained via fitting the $\ln(\Delta R/R_0)$ versus strain curve. The coefficient A is proportional to the number of conducting units within a conducting path but inversely proportional to the number of conducting paths. The coefficient B is associated with the average tunneling distance and the height of the potential barrier between adjacent conducting units. According to eq 2, the coefficients A and B were 1.389 and 6.672, respectively. The derivative of relative change in resistance with respect to the applied strain is equivalent to GF and the value was $9.267 \bullet e^{6.672\varepsilon}$ according to $GF = ABe^{B\varepsilon}$. The GF curves from the fitting equation and experimental data showed good agreement. The linearity is observed in ln (R/R_0) versus strain.

Mechanical and Electrical Hysteresis. Electrical and mechanical hysteresis occurs when the graph of relative resistance change versus strain, as well as the stress−strain curve, does not follow the same path during the loading and unloading phases, thereby exhibiting a deviation. The mechanical and electrical hysteresis of the spongy Ag foam were evaluated by plotting the $\Delta R/R_0$ versus strain curves, with the resistance of each cycle (100th, 500th, 1,000th) set as the initial value. The extent of hysteresis was determined by the width of the hysteresis loop. The areal variation between the loading and unloading states of relative electrical signal change versus strain was quantitatively defined as electrical hysteresis and by the following eq 3:

$$H_E = \frac{|A_L - A_U|}{A_U} \times 100\% \tag{3}$$

where A_L and A_U are the areas of relative electrical signal change versus strain in the loading and unloading states, respectively. Mechanical hysteresis (H_M) was defined as the areal difference under stress−strain curves during loading−unloading cycles and computed by the following eq 4:

$$H_M = \frac{|A_L - A_U|}{A_U} \times 100\% \tag{4}$$

where A_L and A_U are the area under the stress−strain graph in loading and unloading states, respectively. The details of mechanical and electrical hysteresis are shown in Figure S24.

Human Motion Detection. All the human studies were conducted in compliance with the university regulations and approved by the Institutional Review Board (IRB protocol #: 202212−009). The spongy Ag foam was fitted with Cu tape (CST5; Digi-key, Inc.) on both sides to act as electrical connectors and then mounted on various body parts. During measurement, the Cu tapes were linked to a source meter (Keithley 2400; Tektronix, Inc.) in a two-wire setup.

Skin Irritation Testing. Inflammation accompanied by erythema, which changes the concentrations of hemoglobin, is a common response after irritation of the human skin.[61] Line-scan hyperspectral images (hypercube) of the human skin were obtained by using a monochrome camera (GS3-U3−120S6M-C; FLIR), with a slit width of 23 μm and groove density of 150 mm^{-1}. An LED light source with a color temperature of 6,500 K (D65) was used as the illumination source. Spectral calibration of the spectrograph was performed using a xenon calibration light source that emitted multiple narrow peaks at specific wavelengths. A fixed focal length lens (MVL25M1; Navitar) was mainly used to image the skin, with a field of view as small as 10 mm × 10 mm. The same area was imaged with a smartphone camera (iPhone 11 Pro; Apple) to capture RGB images. The spongy Ag foam was applied onto the medial antebrachial cutaneous of the forearm for around 10 min. As a positive control, a 3 M tape was attached to the same area for 10 min. Images were acquired before and after the experiment for hemoglobin content comparison. A mechanical linear scan step was performed at 0.25 mm. The data were acquired using a custom MATLAB interface. A tissue reflectance spectral model was used to extract key hemodynamic parameters from the ground-truth hyperspectral image. The theory of radiative transport and robust approximations (e.g., diffusion, Born, and empirical modeling) was used to model light propagation in tissue. The intensity reflected from a biological sample can be expressed as a function of λ in the visible range:

$$I_R(\lambda) = \left[b_1\left(\frac{\lambda}{\lambda_0}\right)^{b_2} + b_3\left(\frac{\lambda}{\lambda_0}\right)^{-4}\right] \exp[-b_4 \times \{b_5 \times \varepsilon_{HbO_2}(\lambda) + (1 - b_5) \times \varepsilon_{Hb}(\lambda)\}] \tag{5}$$

where b_1, b_2, and b_3 are associated with the scattering (Mie or Rayleigh) contributions at λ_0 = 800 nm, ε_{HbO2} (λ) denotes the absorption coefficient of oxygenated hemoglobin (HbO_2), ε_{Hb} (λ) denotes the absorption coefficient of deoxygenated hemoglobin (H_b), b_4 is the hemoglobin concentration multiplied by the optical path length, and b_5 is the blood oxygen saturation (sPO_2). In the study, the hemoglobin contents multiplied by the optical path length (b_4) was used to indicate the level of skin irritation by eq 5. All fitting parameters were computed by using the simplex search (Nelder−Mead) algorithm.

Cell Viability. The samples were placed into a 24-well plate on the bottom side facing upward. Then, samples were suspended in a 1.5% agarose gel so that the only top layers in the 24-well plate were able to contact the cells. HPAECs were seeded inside the wells with a density of 0.1×10^6 per well in Vascular Cell Basal Medium with an VEGF growth kit (ATCC, PCS-100−041) and then incubated at 37.5 °C with 5% carbon dioxide (CO_2) for 48 h. At each 24 h, MTT (Abcam,

https://doi.org/10.1021/acsami.4c04719
ACS Appl. Mater. Interfaces XXXX, XXX, XXX−XXX

ab211091) and NR (Abcam, ab234039) assays were carried out according to the protocols of each kit. The absorbance was then measured using a microplate reader (Synergy H1, BioTek) at wavelengths of 590 and 540 nm, respectively.

■ ASSOCIATED CONTENT

Supporting Information

The Supporting Information is available free of charge at https://pubs.acs.org/doi/10.1021/acsami.4c04719.

SEM images showcasing the spongy Ag foam structure, emphasizing the presence of perforated micropores, and the percolation networks of Ag NWs acting as internal conducting passages; SEM images and pore size distribution of the PDMS foam in its core and outside; schematic diagram demonstrating the process of patterning the spongy Ag foam through the use of a shadow mask, photographs displaying the resulting patterned spongy Ag foam; 3D FEA results of the spongy Ag foam with a range of porosity under various loading conditions: stretching up to 20%, compression up to 20%, and bending up to 60°; 2D FEA results of the spongy Ag foam under various loading conditions: stretching up to 50%, compression up to 50%, and bending up to 104°; schematic illustration of the spongy Ag foam and control group during stretching and releasing processes; comparison of strain distributions between the spongy Ag foam and the control group; comparison of R and $\Delta R/R_0$ between the spongy Ag foam and the MWCNT foam; The strain-sensing range and $\Delta R/R_0$ of the spongy Ag foam with the different sample size; $\Delta R/R_0$ of the spongy Ag foam with strain according to the concentration of Ag NWs, initial resistance and strain-sensing range of the spongy Ag foam according to the concentration of Ag NWs; SEM images showing cracks and delamination in the control group; $\Delta R/R_0$ of the spongy Ag foam during 2,000 stretching-releasing cycles at 10% (red line), 30% (blue line), and 50% (green line) strains; SEM images of the spongy Ag foam and control group after 1,000 stretching cycles; H_M and H_E of the spongy Ag foam at 10% (red line), 30% (blue line), and 50% (green line) strains; H_M and H_E comparison of the spongy Ag foam and control group; response/recovery time of the spongy Ag foam at 10%, 30%, and 50% strains; $\Delta R/R_0$ observed in the spongy Ag foam during compression and bending; demonstration of LED using the spongy Ag foam, highlighting its selective response to stretching compared to other deformation modes, light intensity changes observed in the spongy Ag foam during compression, bending, and stretching; RGB images of forearm skin area before experiments (control), after applying Spongy Ag Foam, and after applying 3 M Tape are shown on the left column; hemoglobin map measured with hyperspectral line-scanning system are shown on the right column; average hemoglobin contents of a sampled area (a) are shown in bar graph (n = 5); cell viabilit; assay of HPAEC seeded on the spongy Ag foam (red bars) as compared to its bare cells (blue bars) (n = 9) using (a) MTT assay and (b) NR assay; schematic of fabrication setup; photographs of rice cooker setup and the resulting patterned spongy PDMS; the resistance of spongy Ag foam over 14 days; $\Delta R/R_0$ of the spongy Ag foam under (a) 80 °C and (b) 95% relative humidity; schematics of H_E and H_M; comparison of performance results between the spongy Ag foam and other stretchable strain gauges; comparison of porous structure fabrication methods; pore size distribution from SEM image between core and outside of PDMS foam(PDF)

The spongy Ag foam under various deformation modes (MP4)

3D FEA results of the spongy Ag foam under stretching, compression, and bending (MOV)

Selective response of the spongy Ag foam to stretching compared to other deformation modes (MP4)

Demonstration of LED using the spongy Ag foam, showcasing its selective response to stretching compared to other deformation modes (MP4)

Proof-of-concept demonstration showcasing the use of spongy Ag foam on various body parts to detect skin deformations and vibrations (MP4)

Proof-of-concept demonstration of human−robot interaction using a glove with the spongy Ag foam attached to a human hand (MP4)

■ AUTHOR INFORMATION

Corresponding Authors

Dong Rip Kim − *School of Mechanical Engineering, Hanyang University, Seoul 04763, Republic of Korea;* orcid.org/0000-0001-6398-9483; Email: dongrip@hanyang.ac.kr

Baoxing Xu − *Department of Mechanical and Aerospace Engineering, University of Virginia, Charlottesville, Virginia 22903-1738, United States;* orcid.org/0000-0002-2591-8737; Email: bx4c@virginia.edu

Chi Hwan Lee − *Weldon School of Biomedical Engineering and School of Mechanical Engineering, Purdue University, West Lafayette, Indiana 47907, United States; Center for Implantable Devices and School of Materials Engineering, Purdue University, West Lafayette, Indiana 47907, United States;* Present Address: Elmore Family School of Electrical and Computer Engineering, Purdue University, West Lafayette, Indiana 47907, United States; orcid.org/0000-0002-4868-7054; Email: lee2270@purdue.edu

Authors

Seokkyoon Hong − *Weldon School of Biomedical Engineering, Purdue University, West Lafayette, Indiana 47907, United States;* orcid.org/0009-0007-6540-0389

Haozhe Zhang − *Department of Mechanical and Aerospace Engineering, University of Virginia, Charlottesville, Virginia 22903-1738, United States*

Junsang Lee − *Weldon School of Biomedical Engineering, Purdue University, West Lafayette, Indiana 47907, United States; School of Mechanical Engineering, Hanyang University, Seoul 04763, Republic of Korea*

Tianhao Yu − *School of Mechanical Engineering, Purdue University, West Lafayette, Indiana 47907, United States;* orcid.org/0000-0001-9637-352X

Seungse Cho − *Weldon School of Biomedical Engineering, Purdue University, West Lafayette, Indiana 47907, United States*

Taewoong Park − *Weldon School of Biomedical Engineering, Purdue University, West Lafayette, Indiana 47907, United States*

https://doi.org/10.1021/acsami.4c04719
ACS Appl. Mater. Interfaces XXXX, XXX, XXX−XXX

Julia Walsh − *Weldon School of Biomedical Engineering, Purdue University, West Lafayette, Indiana 47907, United States;* orcid.org/0000-0001-6637-7191
Yuhyun Ji − *Weldon School of Biomedical Engineering, Purdue University, West Lafayette, Indiana 47907, United States*
Joshua Jeremiah Kim − *Weldon School of Biomedical Engineering, Purdue University, West Lafayette, Indiana 47907, United States*
Hyowon Lee − *Weldon School of Biomedical Engineering, Purdue University, West Lafayette, Indiana 47907, United States;* orcid.org/0000-0001-7628-1441

Complete contact information is available at: https://pubs.acs.org/10.1021/acsami.4c04719

Author Contributions

[▽]S.H., H.Z., and J.L. contributed equally to this work.

Notes

The authors declare no competing financial interest.

■ ACKNOWLEDGMENTS

This work is funded by the Eli Lilly and Company. C.H.L. acknowledges the Leslie A. Geddes Endowment at Purdue University. B.X. acknowledges support from the Virginia Microelectronics Consortium (VMEC). J.L. acknowledges participation in the 2022 Summer Research Program at Purdue University. J.L. acknowledges funding support from the Ministry of Trade, Industry, and Energy (MOTIE) in Korea, under the Human Resource Development Program for Industrial Innovation (Global) (P0017306; Global Human Resource Development for Innovative Design in Robot and Engineering) supervised by the Korea Institute for Advancement of Technology (KIAT).

■ REFERENCES

(1) Wang, C.; Qi, B.; Lin, M.; Zhang, Z.; Makihata, M.; Liu, B.; Zhou, S.; Huang, Y.-H.; Hu, H.; Gu, Y.; et al. Continuous monitoring of deep-tissue haemodynamics with stretchable ultrasonic phased arrays. *Nat. Biomed. Eng.* **2021**, *5*, 749−758.
(2) Wang, Y.; Lee, S.; Yokota, T.; Wang, H.; Jiang, Z.; Wang, J.; Koizumi, M.; Someya, T. A durable nanomesh on-skin strain gauge for natural skin motion monitoring with minimum mechanical constraints. *Sci. Adv.* **2020**, *6*, No. eabb7043.
(3) Han, F.; Wang, T.; Liu, G.; Liu, H.; Xie, X.; Wei, Z.; Li, J.; Jiang, C.; He, Y.; Xu, F. Materials with tunable optical properties for wearable epidermal sensing in health monitoring. *Adv. Mater.* **2022**, *34*, 2109055.
(4) Shi, X.; Liu, S.; Sun, Y.; Liang, J.; Chen, Y. Lowering internal friction of 0D−1D−2D ternary nanocomposite-based strain sensor by fullerene to boost the sensing performance. *Adv. Funct. Mater.* **2018**, *28*, 1800850.
(5) Wu, S.; Moody, K.; Kollipara, A.; Zhu, Y. Highly Sensitive, Stretchable, and Robust Strain Sensor Based on Crack Propagation and Opening. *ACS Appl. Mater. Interfaces* **2023**, *15*, 1798−1807.
(6) Yin, B.; Liu, X.; Gao, H.; Fu, T.; Yao, J. Bioinspired and bristled microparticles for ultrasensitive pressure and strain sensors. *Nat. Commun.* **2018**, *9*, 5161.
(7) Park, M.; Im, J.; Shin, M.; Min, Y.; Park, J.; Cho, H.; Park, S.; Shim, M.-B.; Jeon, S.; Chung, D.-Y.; et al. Highly stretchable electric circuits from a composite material of silver nanoparticles and elastomeric fibres. *Nat. Nanotechnol.* **2012**, *7*, 803−809.
(8) Jiang, Y.; Ji, S.; Sun, J.; Huang, J.; Li, Y.; Zou, G.; Salim, T.; Wang, C.; Li, W.; Jin, H.; et al. A universal interface for plug-and-play assembly of stretchable devices. *Nature* **2023**, *614*, 456−462.
(9) Yamada, T.; Hayamizu, Y.; Yamamoto, Y.; Yomogida, Y.; Izadi-Najafabadi, A.; Futaba, D. N.; Hata, K. A stretchable carbon nanotube strain sensor for human-motion detection. *Nat. Nanotechnol.* **2011**, *6*, 296−301.
(10) Lipomi, D. J.; Vosgueritchian, M.; Tee, B. C.; Hellstrom, S. L.; Lee, J. A.; Fox, C. H.; Bao, Z. Skin-like pressure and strain sensors based on transparent elastic films of carbon nanotubes. *Nat. Nanotechnol.* **2011**, *6*, 788−792.
(11) Yu, Y.; Nassar, J.; Xu, C.; Min, J.; Yang, Y.; Dai, A.; Doshi, R.; Huang, A.; Song, Y.; Gehlhar, R.; et al. Biofuel-powered soft electronic skin with multiplexed and wireless sensing for human-machine interfaces. *Sci. Rob.* **2020**, *5*, No. eaaz7946.
(12) Gong, S.; Schwalb, W.; Wang, Y.; Chen, Y.; Tang, Y.; Si, J.; Shirinzadeh, B.; Cheng, W. A wearable and highly sensitive pressure sensor with ultrathin gold nanowires. *Nat. Commun.* **2014**, *5*, 3132.
(13) Jung, D.; Lim, C.; Park, C.; Kim, Y.; Kim, M.; Lee, S.; Lee, H.; Kim, J. H.; Hyeon, T.; Kim, D. H. Adaptive Self-Organization of Nanomaterials Enables Strain-Insensitive Resistance of Stretchable Metallic Nanocomposites. *Adv. Mater.* **2022**, *34*, 2200980.
(14) Jung, D.; Lim, C.; Shim, H. J.; Kim, Y.; Park, C.; Jung, J.; Han, S. I.; Sunwoo, S.-H.; Cho, K. W.; Cha, G. D.; et al. Highly conductive and elastic nanomembrane for skin electronics. *Science* **2021**, *373*, 1022−1026.
(15) Kang, D.; Pikhitsa, P. V.; Choi, Y. W.; Lee, C.; Shin, S. S.; Piao, L.; Park, B.; Suh, K.-Y.; Kim, T.-I.; Choi, M. Ultrasensitive mechanical crack-based sensor inspired by the spider sensory system. *Nature* **2014**, *516*, 222−226.
(16) Cheng, X.; Zhang, F.; Bo, R.; Shen, Z.; Pang, W.; Jin, T.; Song, H.; Xue, Z.; Zhang, Y. An anti-fatigue design strategy for 3D ribbon-shaped flexible electronics. *Adv. Mater.* **2021**, *33*, 2102684.
(17) Song, H.; Luo, G.; Ji, Z.; Bo, R.; Xue, Z.; Yan, D.; Zhang, F.; Bai, K.; Liu, J.; Cheng, X.; et al. Highly-integrated, miniaturized, stretchable electronic systems based on stacked multilayer network materials. *Sci. Adv.* **2022**, *8*, No. eabm3785.
(18) Yan, W.; Fuh, H.-R.; Lv, Y.; Chen, K.-Q.; Tsai, T.-Y.; Wu, Y.-R.; Shieh, T.-H.; Hung, K.-M.; Li, J.; Zhang, D.; et al. Giant gauge factor of Van der Waals material based strain sensors. *Nat. Commun.* **2021**, *12*, 2018.
(19) Seyedin, S.; Uzun, S.; Levitt, A.; Anasori, B.; Dion, G.; Gogotsi, Y.; Razal, J. M. MXene composite and coaxial fibers with high stretchability and conductivity for wearable strain sensing textiles. *Adv. Funct. Mater.* **2020**, *30*, 1910504.
(20) Ning, C.; Cheng, R.; Jiang, Y.; Sheng, F.; Yi, J.; Shen, S.; Zhang, Y.; Peng, X.; Dong, K.; Wang, Z. L. Helical fiber strain sensors based on triboelectric nanogenerators for self-powered human respiratory monitoring. *ACS Nano* **2022**, *16*, 2811−2821.
(21) Lee, J.; Shin, S.; Lee, S.; Song, J.; Kang, S.; Han, H.; Kim, S.; Kim, S.; Seo, J.; Kim, D. Highly sensitive multifilament fiber strain sensors with ultrabroad sensing range for textile electronics. *ACS Nano* **2018**, *12*, 4259−4268.
(22) Tian, K.; Pan, Q.; Deng, H.; Fu, Q. Shear induced formation and destruction behavior of conductive networks in nickel/polyurethane composites during strain sensing. Compos. *Composites, Part A* **2020**, *130*, 105757.
(23) Tian, K.; Chen, C.; Li, Q.; Cao, X.; Chen, X.; Fu, Q.; Deng, H. Evaporation-Induced Closely-Packing of Core−Shell PDMS@ Ag Microspheres Enabled Stretchable Conductor with Ultra-High Conductance. *Adv. Funct. Mater.* **2023**, *33*, 2308799.
(24) Tian, K.; Hu, D.; Wei, Q.; Fu, Q.; Deng, H. Recent progress on multifunctional electromagnetic interference shielding polymer composites. *J. Mater. Sci. Technol.* **2023**, *134*, 106−131.
(25) Yang, J. C.; Mun, J.; Kwon, S. Y.; Park, S.; Bao, Z.; Park, S. Electronic skin: Recent progress and future prospects for skin-attachable devices for health monitoring, robotics, and prosthetics. *Adv. Mater.* **2019**, *31*, 1904765.
(26) Amjadi, M.; Kyung, K. U.; Park, I.; Sitti, M. Stretchable, skin-mountable, and wearable strain sensors and their potential applications: A review. *Adv. Funct. Mater.* **2016**, *26*, 1678−1698.
(27) Chen, H. Y.; Chen, Z. Y.; Mao, M.; Wu, Y. Y.; Yang, F.; Gong, L. X.; Zhao, L.; Cao, C. F.; Song, P.; Gao, J. F.; et al. Self-adhesive polydimethylsiloxane foam materials decorated with MXene/cellulose

nanofiber interconnected network for versatile functionalities. *Adv. Funct. Mater.* **2023**, *33*, 2304927.
(28) Tian, K.; Qin, T.; Li, Q.; Chen, C.; Dai, Z.; Wei, X.; Fu, Q.; Deng, H. Stretchable Multifunctional Polydimethylsiloxane Composites with Cage-Like Conductive Architecture for Integrated Thermosensitive and Electromagnetic Interference Shielding Performance. *Adv. Funct. Mater.* **2024**, 2400288.
(29) Park, J.; Wang, S.; Li, M.; Ahn, C.; Hyun, J. K.; Kim, D. S.; Kim, D. K.; Rogers, J. A.; Huang, Y.; Jeon, S. Three-dimensional nanonetworks for giant stretchability in dielectrics and conductors. *Nat. Commun.* **2012**, *3*, 916.
(30) Cho, D.; Park, J.; Kim, J.; Kim, T.; Kim, J.; Park, I.; Jeon, S. Three-dimensional continuous conductive nanostructure for highly sensitive and stretchable strain sensor. *ACS Appl. Mater. Interfaces* **2017**, *9*, 17369−17378.
(31) Wu, S.; Zhang, J.; Ladani, R. B.; Ravindran, A. R.; Mouritz, A. P.; Kinloch, A. J.; Wang, C. H. Novel electrically conductive porous PDMS/carbon nanofiber composites for deformable strain sensors and conductors. *ACS Appl. Mater. Interfaces* **2017**, *9*, 14207−14215.
(32) Hong, S.; Park, J.; Jeon, S. G.; Kim, K.; Park, S. H.; Shin, H. S.; Kim, B.; Jeon, S.; Song, J. Y. Monolithic Bi 1.5 Sb 0.5 Te 3 ternary alloys with a periodic 3D nanostructure for enhancing thermoelectric performance. *J. Mater. Chem. C* **2017**, *5*, 8974−8980.
(33) Zhang, Y.; Zhang, T.; Huang, Z.; Yang, J. A new class of electronic devices based on flexible porous substrates. *Adv. Sci.* **2022**, *9*, 2105084.
(34) Liu, Z.; Zheng, Y.; Jin, L.; Chen, K.; Zhai, H.; Huang, Q.; Chen, Z.; Yi, Y.; Umar, M.; Xu, L.; et al. Highly breathable and stretchable strain sensors with insensitive response to pressure and bending. *Adv. Funct. Mater.* **2021**, *31*, 2007622.
(35) Xu, R.; Zeng, Z.; Lei, Y. Well-defined nanostructuring with designable anodic aluminum oxide template. *Nat. Commun.* **2022**, *13*, 2435.
(36) Yan, D.; Chang, J.; Zhang, H.; Liu, J.; Song, H.; Xue, Z.; Zhang, F.; Zhang, Y. Soft three-dimensional network materials with rational bio-mimetic designs. *Nat. Commun.* **2020**, *11*, 1180.
(37) Dong, Z.; Cui, H.; Zhang, H.; Wang, F.; Zhan, X.; Mayer, F.; Nestler, B.; Wegener, M.; Levkin, P. A. 3D printing of inherently nanoporous polymers via polymerization-induced phase separation. *Nat. Commun.* **2021**, *12*, 247.
(38) Tian, L.; Zimmerman, B.; Akhtar, A.; Yu, K. J.; Moore, M.; Wu, J.; Larsen, R. J.; Lee, J. W.; Li, J.; Liu, Y.; et al. Large-area MRI-compatible epidermal electronic interfaces for prosthetic control and cognitive monitoring. *Nat. Biomed. Eng.* **2019**, *3*, 194−205.
(39) Wang, Y.; Li, M.; Chang, J.-K.; Aurelio, D.; Li, W.; Kim, B. J.; Kim, J. H.; Liscidini, M.; Rogers, J. A.; Omenetto, F. G. Light-activated shape morphing and light-tracking materials using biopolymer-based programmable photonic nanostructures. *Nat. Commun.* **2021**, *12*, 1651.
(40) Kim, H.; Kim, M. K.; Jang, H.; Kim, B.; Kim, D. R.; Lee, C. H. Sensor-Instrumented Scaffold Integrated with Microporous Sponge-like Ultrabuoy for Long-Term 3D Mapping of Cellular Behaviors and Functions. *ACS Nano* **2019**, *13*, 7898−7904.
(41) Dahiya, A. S.; Gil, T.; Thireau, J.; Azemard, N.; Lacampagne, A.; Charlot, B.; Todri-Sanial, A. 1D nanomaterial-based highly stretchable strain sensors for human movement monitoring and human−robotic interactive systems. *Adv. Electron. Mater.* **2020**, *6*, 2000547.
(42) Amjadi, M.; Pichitpajongkit, A.; Lee, S.; Ryu, S.; Park, I. Highly stretchable and sensitive strain sensor based on silver nanowire−elastomer nanocomposite. *ACS Nano* **2014**, *8*, 5154−5163.
(43) Wang, X.; Li, J.; Song, H.; Huang, H.; Gou, J. Highly stretchable and wearable strain sensor based on printable carbon nanotube layers/polydimethylsiloxane composites with adjustable sensitivity. *ACS Appl. Mater. Interfaces* **2018**, *10*, 7371−7380.
(44) Ahuja, P.; Akiyama, S.; Ujjain, S. K.; Kukobat, R.; Vallejos-Burgos, F.; Futamura, R.; Hayashi, T.; Kimura, M.; Tomanek, D.; Kaneko, K. A water-resilient carbon nanotube based strain sensor for monitoring structural integrity. *J. Mater. Chem. A* **2019**, *7*, 19996−20005.
(45) Kim, K. H.; Jang, N. S.; Ha, S. H.; Cho, J. H.; Kim, J. M. Highly sensitive and stretchable resistive strain sensors based on micro-structured metal nanowire/elastomer composite films. *Small* **2018**, *14*, 1704232.
(46) Lu, N.; Lu, C.; Yang, S.; Rogers, J. Highly sensitive skin-mountable strain gauges based entirely on elastomers. *Adv. Funct. Mater.* **2012**, *22*, 4044−4050.
(47) Kim, K. K.; Hong, S.; Cho, H. M.; Lee, J.; Suh, Y. D.; Ham, J.; Ko, S. H. Highly sensitive and stretchable multidimensional strain sensor with prestrained anisotropic metal nanowire percolation networks. *Nano Lett.* **2015**, *15*, 5240−5247.
(48) Cai, Y.; Shen, J.; Dai, Z.; Zang, X.; Dong, Q.; Guan, G.; Li, L. J.; Huang, W.; Dong, X. Extraordinarily Stretchable All-Carbon Collaborative Nanoarchitectures for Epidermal Sensors. *Adv. Mater.* **2017**, *29*, 1606411.
(49) Shen, G.; Chen, B.; Liang, T.; Liu, Z.; Zhao, S.; Liu, J.; Zhang, C.; Yang, W.; Wang, Y.; He, X. Transparent and stretchable strain sensors with improved sensitivity and reliability based on Ag NWs and PEDOT: PSS patterned microstructures. *Adv. Electron. Mater.* **2020**, *6*, 1901360.
(50) Yu, Y.; Zhai, Y.; Yun, Z.; Zhai, W.; Wang, X.; Zheng, G.; Yan, C.; Dai, K.; Liu, C.; Shen, C. Ultra-stretchable porous fiber-shaped strain sensor with exponential response in full sensing range and excellent anti-interference ability toward buckling, torsion, temperature, and humidity. *Adv. Electron. Mater.* **2019**, *5*, 1900538.
(51) Haake, A.; Tutika, R.; Schloer, G. M.; Bartlett, M. D.; Markvicka, E. J. On-Demand Programming of Liquid Metal-Composite Microstructures through Direct Ink Write 3D Printing. *Adv. Mater.* **2022**, *34*, 2200182.
(52) Kwon, D.; Lee, T.-I.; Shim, J.; Ryu, S.; Kim, M. S.; Kim, S.; Kim, T.-S.; Park, I. Highly sensitive, flexible, and wearable pressure sensor based on a giant piezocapacitive effect of three-dimensional microporous elastomeric dielectric layer. *ACS Appl. Mater. Interfaces* **2016**, *8*, 16922−16931.
(53) Wu, S.; Peng, S.; Han, Z. J.; Zhu, H.; Wang, C. H. Ultrasensitive and stretchable strain sensors based on mazelike vertical graphene network. *ACS Appl. Mater. Interfaces* **2018**, *10*, 36312−36322.
(54) Muth, J. T.; Vogt, D. M.; Truby, R. L.; Mengüç, Y.; Kolesky, D. B.; Wood, R. J.; Lewis, J. A. Embedded 3D printing of strain sensors within highly stretchable elastomers. *Adv. Mater.* **2014**, *26*, 6307−6312.
(55) Lee, J.; Lim, M.; Yoon, J.; Kim, M. S.; Choi, B.; Kim, D. M.; Kim, D. H.; Park, I.; Choi, S.-J. Transparent, flexible strain sensor based on a solution-processed carbon nanotube network. *ACS Appl. Mater. Interfaces* **2017**, *9*, 26279−26285.
(56) Yin, R.; Wang, D.; Zhao, S.; Lou, Z.; Shen, G. Wearable sensors-enabled human−machine interaction systems: from design to application. *Adv. Funct. Mater.* **2021**, *31*, 2008936.
(57) Tan, C.; Dong, Z.; Li, Y.; Zhao, H.; Huang, X.; Zhou, Z.; Jiang, J.-W.; Long, Y.-Z.; Jiang, P.; Zhang, T.-Y.; et al. A high performance wearable strain sensor with advanced thermal management for motion monitoring. *Nat. Commun.* **2020**, *11*, 3530.
(58) Abramson, A.; Chan, C. T.; Khan, Y.; Mermin-Bunnell, A.; Matsuhisa, N.; Fong, R.; Shad, R.; Hiesinger, W.; Mallick, P.; Gambhir, S. S.; et al. A flexible electronic strain sensor for the real-time monitoring of tumor regression. *Sci. Adv.* **2022**, *8*, No. eabn6550.
(59) Qaiser, N.; Al-Modaf, F.; Khan, S. M.; Shaikh, S. F.; El-Atab, N.; Hussain, M. M. A robust wearable point-of-care CNT-based strain sensor for wirelessly monitoring throat-related illnesses. *Adv. Funct. Mater.* **2021**, *31*, 2103375.
(60) Amit, M.; Chukoskie, L.; Skalsky, A. J.; Garudadri, H.; Ng, T. N. Flexible pressure sensors for objective assessment of motor disorders. *Adv. Funct. Mater.* **2020**, *30*, 1905241.
(61) de Melo, G. D.; Lazarini, F.; Levallois, S.; Hautefort, C.; Michel, V.; Larrous, F.; Verillaud, B.; Aparicio, C.; Wagner, S.; Gheusi, G.; et al. COVID-19−related anosmia is associated with viral persistence

https://doi.org/10.1021/acsami.4c04719
ACS Appl. Mater. Interfaces XXXX, XXX, XXX−XXX

and inflammation in human olfactory epithelium and brain infection in hamsters. *Sci. Transl. Med.* **2021**, *13*, No. eabf8396.

https://doi.org/10.1021/acsami.4c04719
ACS Appl. Mater. Interfaces XXXX, XXX, XXX−XXX